PROCEEDINGS, 41st Workshop on Geothermal Reservoir Engineering
Stanford University, Stanford, California, February 22-24, 2016
SGP-TR-209

Numerical Modeling of Flow-Mechanics Coupling in a Fractured Reservoir with Porous Matrix

Rajdeep Deb and Patrick Jenny

Institute of Fluid Dynamics, ETH Zurich

debr@ethz.ch

Keywords: Slip failure, geomechanics, fractures, poroelasticity

ABSTRACT

Poro-mechanical processes play an important role for fracture aperture changes and micro-seismic activities during water injection in enhanced geothermal systems (EGS). In order to study the poro-mechanics of EGS, a finite volume method based on discrete fracture manifolds embedded in a continuum matrix domain has been developed. For the coupling between stress and fluid pressure in the matrix domain, an unconditionally stable fixed stress scheme is employed, in which the geo-mechanical and flow problems are solved sequentially. In order to get accurate fracture slip solutions and displacements within the matrix, special basis functions were introduced. The degree of freedom associated with these basis functions are computed by requiring stress equilibrium and by honoring the Coulomb friction law. Finite sized fracture segments are used to estimate the shear failure criterion and the subsequent evolution of slip and aperture. Numerical investigations of micro-seismic activities show that the moment magnitude against frequency closely follows the Gutenberg-Richter law. While numerical convergence of slip and pressure solutions is achieved, the smallest size of micro-seismic events depends on the fracture resolution.

1. INTRODUCTION

The poro-mechanical problem of modeling coupled flow and mechanics plays an important role in reservoir engineering. In the case of fractured reservoirs, which is typical for geothermal systems, shear slip plays a critical role from both physical and economical view points. Reservoirs with fractures of different scales are very difficult to model; primarily due to the geometrical complexity. A simplified modeling approach in this regard is to consider the large fractures as discrete low dimensional manifold in a background reservoir matrix and to account for the small fractures by effective damaged matrix properties. Flow in such a damaged matrix is subjected to poro-elastic effects, which therefore should be considered along with flow induced shear failures.

For computational simulations of coupled flow and mechanics in fractured reservoirs computationally efficient models and solution algorithms are crucial. Obviously it is desirable to reduce the number of degrees of freedom (dof) and to employ efficient linear solvers to compute the solutions of the still huge linearized discrete problems. The linear solvers used for such poro-mechanical coupling can be divided into two categories, that is, into direct and iterative solvers. Direct solvers are easier to implement, but require a lot of memory and have an unfavorable computational complexity. Therefore, for reservoir simulations typically iterative solvers are used [2,3,4,5]. In this regard, the approach by Kim et al. [3], which is also known as fixed stress solution scheme, is of particular interest. In this method, the flow and mechanics problems are solved sequentially in an iterative way until a desired accuracy is achieved. For their finite element/finite volume code, Castelletto et al. [1] have developed an efficient iterative linear solver based on a Schur complement and Richardson iterations. In this paper, the same fixed stress approach is used in a pure finite volume set up for coupled flow and mechanics, but the iterative solver strategy exploits the elliptic structure of the block sub-matrices for the mechanics solver and therefore a multigrid method for both flow and mechanics can be employed. However, shear failure along the fracture manifolds has a negative impact on the convergence rate. This problem is overcome with a domain decomposition strategy and a Gauss-Seidel preconditioner. Further, the use of special, discontinuous basis functions to accurately account for shear slip along fracture manifolds allows for consistent solutions independent of grid orientation relative to the fracture manifolds.

The paper is organized as follows. In the next section, the governing equations and closures for coupled flow and mechanics as well as the fixed stress scheme for coupling are introduced. Section 3 deals with the efficient iterative solution of the linearized discrete problem including shear failures. In section 4, comparisons between numerical results and analytical solutions of the Mandel problem are presented, and in section 5 a coupled problem with a single fracture is investigated. Finally, the paper closes with some conclusions.

2. PROBLEM DESCRIPTION AND MODELING

The poro-elastic problem with incompressible fluid can be described by a set of coupled equations, that is, by

$$\frac{1}{M}\frac{\partial P}{\partial t} + b\frac{\partial \varepsilon_v}{\partial t} - \nabla\cdot\left(\frac{k}{m}\nabla P\right) = q \tag{1}$$

$$\tilde{\sigma} = \lambda\left(\nabla\cdot\vec{u}\right)\tilde{I} + G(\nabla\vec{u} + \nabla\vec{u}^T) - \left(bP\right)\tilde{I} \tag{2}$$

$$\nabla\cdot\tilde{\sigma} = 0 \tag{3}$$

which are solved in the damaged matrix domain. Equation (1) describes the flow evolution in the damaged matrix, which is derived from mass balance. The rate of matrix porosity change (the first two terms) is a function of pressure rate of change and change in

volumetric strain. The Biot modulus is denoted by M, b is the Biot coefficient and P the fluid pressure. Further, κ is the effective permeability, μ the fluid viscosity, q some volumetric fluid source and u denotes the matrix displacement. The effect of pore fluid pressure on the mechanics problem is taken into account via the modified constitutive poro-elastic relation (2) between stress and strain. Equation (3) represents the mechanical equilibrium, which relates mechanical consolidation to the dissipation of fluid pressure. The mechanical stress change affects the total pore volume and therefore also the mass balance equation (1).

From a numerical point of view, this coupling imposes a strong restriction on the time step size and thus negatively affects the computational efficiency of the iterative solution strategy. With the fixed-stress approach during the inner iterative pressure updates, each time after mechanical equilibrium is computed, proved to be unconditionally stable [3] and thus the choice of the time step size can be made based on accuracy considerations only. In summary, this technique relies on incorporating the effect of volume strain rate of change in such a way that total volumetric stress is conserved during each iterative update. The net volumetric stress is defined as

$$\sigma_v = \tilde{K}\nabla\cdot\vec{u} - bP \tag{4}$$

The choice of a suitable modulus of elasticity ($\tilde{K}$) in this case depends on the problem dimension; in a two-dimensional set up the plain strain modulus of elasticity K_{2d} is used which is defined as

$$K_{2d} = \frac{G}{(1-2\nu)}, \tag{5}$$

where ν is the Poisson constant. While the volumetric strain rate of change, which is required in the discretized mass balance equation, is estimated during a numerical time step, it is assumed that the stress does not change during an inner iterative step. This leads to the estimate

$$\int b\left(\nabla\cdot\vec{u}\right)_{k+1}^{n} dV = \int\left(b\left(\nabla\cdot\vec{u}\right)_{k}^{n} + \frac{b^2}{K_{2d}}\left(P_{k+1}^{n} - P_{k}^{n}\right)\right) dV \tag{6}$$

of the new average volumetric strain in a finite volume cell after an iterative pressure update. The subscript k denotes the k^{th} iterative step and the superscript n denotes the n^{th} time step. The use of an iterative strategy allows to develop separate linear solvers for flow and mechanics. Further details are provided in the following section.

3. LINEAR SOLVER FOR THE PORO-ELASTIC PROBLEM

Both flow and mechanics problems are discretized using a finite volume method. The domain is divided into finite volume cells and then for each cell the volume averaged equations are solved. The flux terms (mainly the force fluxes) of the mechanical equilibrium equation (3) and the fluxes of the flow problem (1) are estimated based on the stored grid point pressure and displacement values. The staggered grid approach, in which pressure and displacement values are stored at alternate locations as shown in figure 1, is very well suited for the considered coupling approach. The pressure and dislocation nodes are located at the boundaries of the control volumes used for the mechanics and flow problems, respectively, and therefore can directly be used to perform the integration.

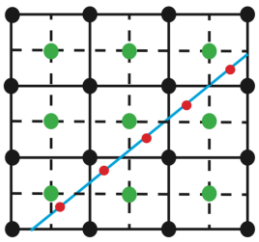

Figure 1: Illustration of the staggered grid arrangement used to solve the coupled problem. Green and black nodes represent the locations of pressure and displacement solutions, respectively. Further, an embedded fracture is depicted (blue line) with one degree of freedom for each fracture segment to account for fracture pressure and slip.

The discretized flow problem can be written in algebraic form as

$$M\dot{P} + B_2\dot{U} + TP = g, \tag{7}$$

where M is the capacity matrix, as defined by Castelletto et. al. [1], and B_1 the poro-mechanics matrix. A backward Euler time stepping scheme for flow-mechanics problem then leads to

$$\begin{bmatrix} A & B_1 \\ B_2 & C \end{bmatrix}\begin{bmatrix} U^n \\ P^n \end{bmatrix} = \begin{bmatrix} f \\ g \end{bmatrix}. \tag{8}$$

Instead of solving the whole linear system directly, as previously described, it is solved sequentially using the fixed stress approach. One iteration consists of the following two operations:

$$AU^n_{k+1} = f - B_1 P^n_k, \tag{9}$$

$$CP^n_{k+1} = g - B_2 U^n_{k+1}. \tag{10}$$

First, the mechanical equilibrium equation (9) is solved using the previous pressure solution and then the discretized mass balance equation (10) is solved with the updated displacement field while considering a conserved volumetric stress as given by equation (4). These two steps are repeated until convergence is achieved; then P^n and U^n are set to the values of P^n_{k+1} and U^n_{k+1}. Note that this sequential iterative strategy allows for different linear solvers for the flow and mechanics problems. For example, C is an elliptic operator with diagonal dominance and therefore the corresponding system (10) for the new pressure values can be solved efficiently with a multigrid method. The operator *A*, however, does not have a diagonal dominant structure, but it can be arranged as

$$A = \begin{bmatrix} A_{xx} & A_{xy} \\ A_{xy} & A_{yy} \end{bmatrix}, \tag{11}$$

where each block A_{ij} accounts for the contribution of the j^{th} component of the displacement vector to the force balance along the i^{th} direction. Also, both A_{xx} and A_{yy} are diagonal dominant, which brings multigrid methods back in business, if the linear systems are solved in a sequential iterative way as

$$A_{xx} U^n_{x,k,J+1} = f_x - A_{xy} U^n_{y,k,J}, \tag{12}$$

$$A_{yy} U^n_{y,k,J+1} = f_y - A_{xy} U^n_{x,k,J+1}. \tag{13}$$

A new iterative strategy was developed here, in which each of the linear systems (12) and (13) are solved separately using a multigrid method. The algorithm

$$\begin{aligned} &do \\ &\quad A_{xx} U^n_{x,k,J+1} = f_x - A_{xy} U^n_{y,k,J} \\ &\quad A_{yy} U^n_{y,k,J+1} = f_y - A_{xy} U^n_{x,k,J+1} \\ &\quad R = \left\| \begin{bmatrix} f_x & f_y \end{bmatrix}^T - A \begin{bmatrix} U^n_{x,k,J+1} & U^n_{y,k,J+1} \end{bmatrix}^T \right\| \\ &until (R < tolerance) \end{aligned} \tag{14}$$

describes the iterative linear solver, which is applied to the mechanics problem. Convergence is achieved once the residual *R* is reduced below a specified tolerance.

The presence of fractures embedded in a matrix generally leads to preferential flow paths. Tightly coupled to these flow paths, pressure signals propagate and lead to seismic events and shear failure, which alter the stress field. While in our previous model [6,7] only elastic stress-strain relations have been considered, in this paper poro-elastic effects are taken into account.

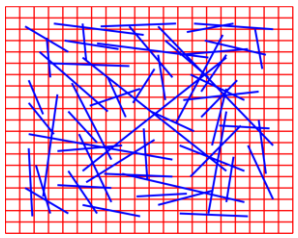

Figure 2: The figure depicts a typical fractured domain with discrete fracture manifolds (blue lines) projected onto a Cartesian finite volume mesh.

Figure 2 depicts a typical fractured domain with discrete fracture manifolds (blue lines) projected onto a Cartesian finite volume mesh is depicted. An illustration of the various dof in the case of one embedded fracture is shown in figure 1; red, green and black dots represent slip and fluid pressure in the fracture segments, matrix displacement, and fluid pressure in the matrix, respectively. In order to accurately account for displacement in the vicinity of fracture manifolds, discontinuous basis functions have been introduced [13]. It is a

key property of these special basis functions that they ensure continuity of the displacement gradient across fractures, which greatly simplifies the calculations of traction and compressive forces without requiring additional constraints. The failure criterion, which is consulted for each fracture segments, is given as

$$t > \mu_s(s - P_f)\,, \tag{15}$$

Equation (15) represents the static friction limit for shear failure depending on fracture pressure and net compressive force obtained from the normal stress due to poro-elastic deformation. If this criterion is fulfilled, then the corresponding fracture segment is subjected to shear failure, that is, a new irreversible slip solution is sought, such that mechanical equilibrium is achieved under dynamic friction conditions:

$$t = \mu_d(s - P_f)\,, \tag{16}$$

Since the fully coupled poro-elastic problem is solved, equations (1) and (3) have to be satisfied. The poro-elastic constitutive law given by equation (2) is satisfied for the elastic part of the displacement field. In the discrete case, the force constraint is obtained by integrating the stress field over all individual fracture segments. As a consequence, in case of failure, the equations (8) has to be replaced by

$$\begin{bmatrix} A_{UU} & A_{SU} & B_1 \\ B_{US} & B_{SS} & C_{PS} \\ B_2 & B_{SP} & C \end{bmatrix} \begin{bmatrix} U^n \\ S^n \\ P^n \end{bmatrix} = \begin{bmatrix} f \\ f_S \\ g \end{bmatrix}. \tag{17}$$

The sub-matrices A_{UU} and A_{SU} in equation (17) represent the contributions of elastic displacement and slip to the force balance. Further, sub-matrix B_{SP} accounts for the contribution of slip to the volumetric strain, which is required in the flow equation. Finally, the sub-matrices B_{US}, B_{SS} and C_{PS} account for the contributions of elastic displacement, slip and fluid pressure to the force constraint equation (16). A similar sequential scheme as previously introduced for the case without failure is devised here for the general case, that is, pressure and displacement fields are iteratively updated by solving the equations

$$A_{UU}U^n_{k+1} + A_{SU}S^n_{k+1} = f - B_1P^n_k, \tag{18}$$

$$B_{US}U^n_{k+1} + B_{SS}S^n_{k+1} = f_S - C_{PS}P^n_k \text{ and} \tag{19}$$

$$CP^n_{k+1} = g - B_2U^n_{k+1} - B_{SP}S^n_{k+1}. \tag{20}$$

The pressure field can be updated using the fixed stress approach based on the current iterative displacement and slip solutions. However, the solver for the mechanics problem requires modification compared to the one described in the previous section, since due to the sub-matrices A_{SU} and B_{US} diagonal dominance is lost. In order to solve this ill-conditioned system, the sequential iterative procedure

$$A_{UU}U^n_{k,J+1} = f - B_1P^n_k - A_{SU}S^n_{k,J}, \tag{21}$$

$$B_{SS}S^n_{k,J+1} = f_S - C_{PS}P^n_k - B_{US}U^n_{k,J+1} \tag{22}$$

is employed. To enhance the convergence rate, at the beginning of each iteration a number of Gauss-Seidel steps are performed within a local subdomain arranged around the failing segments. Pre-conditioning the solution in this way proved to be very effective and once the residual is reduced below a specified tolerance, U^n_{k+1} and S^n_{k+1} are set to the values of $U^n_{k,J+1}$ and $S^n_{k,J+1}$ respectively.

4. VALIDATION WITH ANALYTICAL SOLUTION OF THE MANDEL PROBLEM

Analytical solutions of the Mandel problem [9] are used to study the performance of the numerical solution algorithm for coupled poro-mechanical and flow problems without fractures. Figure 3 shows the rectangular poro-elastic domain with no-flow conditions at the top and bottom boundaries; constant fluid pressure is applied at the left and right boundaries. After starting the experiment, a compressive force *F* per unit length is applied on the top and bottom boundaries, which leads to an increase of fluid pressure.

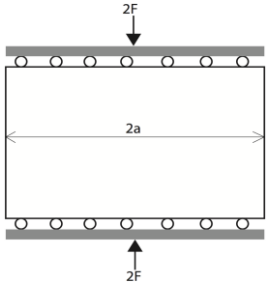

Figure 3: Geometry of the Mandel problem.

Initially, the vertical boundaries are not yet effected by the increasing pressure and thus the amount of fluid in the domain remains constant. The corresponding undrained pressure rise within the domain is given analytically as

$$P_0\left(\vec{x},0\right)=\frac{1}{3a}B\left(1+\nu_u\right)F, \tag{23}$$

where B is the Skempton coefficient and

$$\eta_u=\left[3\eta+bB\left(1-2\eta\right)\right]/\left[3-bB\left(1-2\eta\right)\right]\ . \tag{24}$$

the undrained Poisson ratio (ν is the regular Poisson ratio). At a later time, once the initial, sudden pressure increase P_0 leads to mass fluxes across the vertical boundaries, drained conditions establish. The drained solution of the Mandel problem is obtained from [8] and reads

$$P\left(x,y,t\right)=2P_0\sum_{n=1}^{\infty}\frac{\sin(\alpha_n)}{(\alpha_n-\sin(\alpha_n)\cos(\alpha_n))}\left(\cos\left(\frac{\alpha_n x}{a}\right)-\cos(\alpha_n)\right)\exp\left(-\frac{\alpha_n^2 c_f t}{a^2}\right)\ , \tag{25}$$

$$u_x\left(x,y,t\right)=\left[\frac{\eta F}{2Ga}-\frac{\eta_u F}{Ga}\sum_{n=1}^{\infty}\frac{\sin(\alpha_n)\cos(\alpha_n)}{(\alpha_n-\sin(\alpha_n)\cos(\alpha_n))}\exp\left(-\frac{\alpha_n^2 c_f t}{a^2}\right)\right]x$$

$$+\frac{F}{G}\sum_{n=1}^{\infty}\frac{\cos(\alpha_n)}{(\alpha_n-\sin(\alpha_n)\cos(\alpha_n))}\sin\left(\frac{\alpha_n x}{a}\right)\exp\left(-\frac{\alpha_n^2 c_f t}{a^2}\right)\ \text{and} \tag{26}$$

$$u_y\left(x,y,t\right)=\left[-\frac{(1-\eta)F}{2Ga}+\frac{(1-\eta_u)F}{Ga}\sum_{n=1}^{\infty}\frac{\sin(\alpha_n)\cos(\alpha_n)}{(\alpha_n-\sin(\alpha_n)\cos(\alpha_n))}\exp\left(-\frac{\alpha_n^2 c_f t}{a^2}\right)\right]y, \tag{27}$$

where c_f represent and effective fluid diffusivity (defined below) and α_n are the positive solutions of

$$\tan(\alpha_n)=\frac{(1-\eta)}{(\eta_u-\eta)}\alpha_n\ . \tag{28}$$

As described by Castelletto et. al. [1], the characteristic parameters of the Mandel problem are

$$K_v=2G\frac{(1-\eta)}{(1-2\eta)}\ , \tag{29}$$

$$c_f=(k/\eta)M\frac{K_v}{(K_v+b^2M)} \tag{30}$$

$$t_{nd}=l_c^2/c_f, \tag{31}$$

where *lc* is the characteristic length scale, which is equal to a in this case. Note that t_{nd} defines the characteristic time scale. The coupling strength between flow and mechanics can be quantified by the dimensionless parameter

$$t_c=\left(b^2M/K_v\right). \tag{32}$$

Both, experimental observations by [9] and the corresponding analytical solutions show similar non-monotonous pressure evolutions in the central region of the domain. During a short initial period the pressure rises above the maximum undrained pore pressure and then gradually approaches the pressure value imposed at the vertical boundaries. This phenomenon of overpressure buildup is also called the Mandel-Cryer effect [8]. Here, two cases of the Mandel problem with different coupling strengths are considered. Numerical results, i.e. the pressure evolution in the center of the domain, are depicted in figure 4 along with the corresponding analytical solutions; very good agreement can be observed.

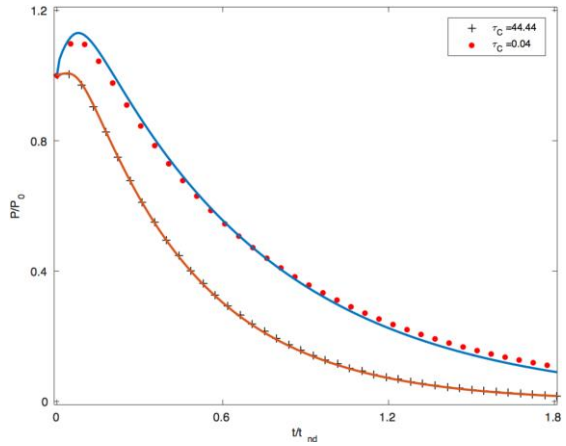

Figure 4: Pressure evolution in the center of the domain for two cases of the Mandel problem with different coupling strengths are considered. Symbols represent the numerical results, while the lines depict the analytical solutions.

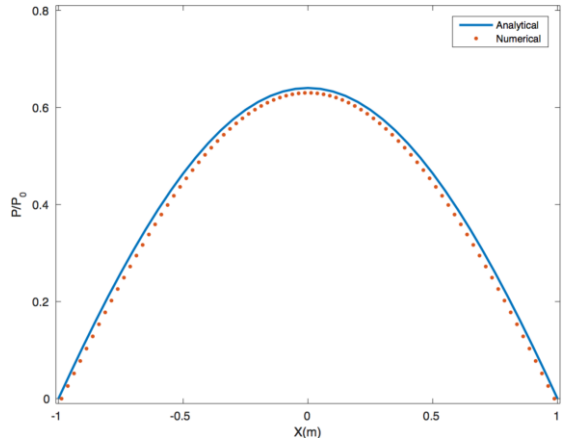

Figure 5: Pressure profile along the horizontal center line of the Mandel problem with coupling strength 44.44 at time t = 0.6t_{nd}. Symbols represent the numerical result, while the line depicts the analytical solution.

5. STUDIES OF FLOW IN POROUS MATRIX WITH FRACTURES

Numerical simulations of flow in a poro-elastic matrix with a single embedded fracture have been performed and investigated. The geometry of the domain and the stress boundary conditions are depicted in figure 6. The domain size is 1000m x 1000m. The initial pressure is 40 MPa and water is injected at the center of the domain at a pressure of 44 MPa.

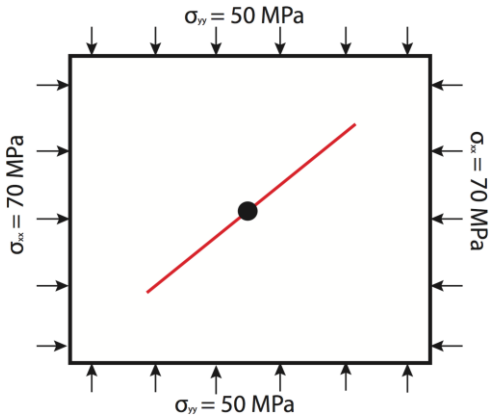

Figure 6: Geometry of the test case with a single fracture (red line) and injection at the center (black point). Also indicated by arrows are the stress boundary conditions.

The dependence of hydraulic aperture is modeled here as suggested by McClure and Horne [10]. The pore volume dependence on total compressive stress is obtained in a simplified way from the work of Wills-Richards et al. [12]. The seismic moment magnitude due to shear failure is denoted as M_w and is defined in the paper of Hanks and Kanimori [11]. Further concise details of these three models,

which are used here, can be found in Deb and Jenny [7]. All fracture and matrix properties are given in table 1, from which a problem timescale of 10^5 sec, based on equation (31), can be estimated.

parameters	values	unit
E_0	1	mm
b_0	0.5	mm
s_{max}	5	mm
μ	8.9e-4	Pa*Sec
κ	5e-14	m^2
M	15000	MPa
b	0.1	
G	10000	MPa
λ	2500	MPa
ν	0.1	
ϕ^d	0.1	%

Table 1: Parameters of flow and stress field solvers.

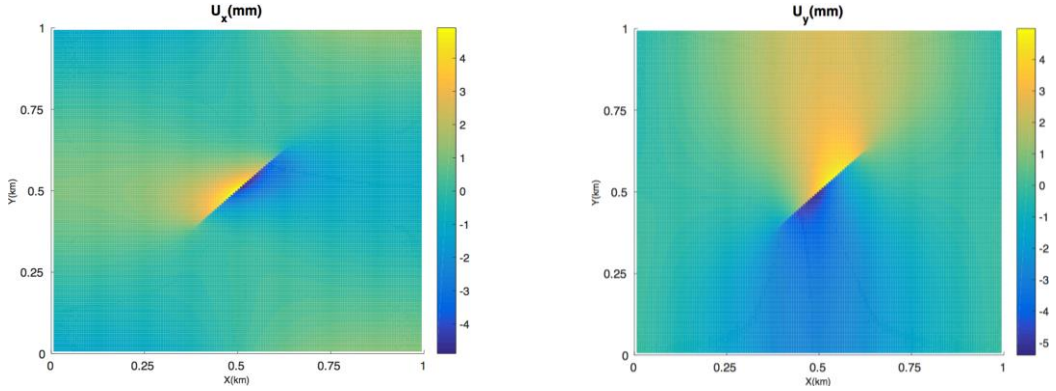

Figure 7: Numerical simulations of poro-elastic flow evolution (t = 1.7x10^4 sec after injection). Horizontal and vertical displacement maps (with respect to the solution with an elastic matrix and same stress boundary conditions) are shown in the left and right figures, respectively.

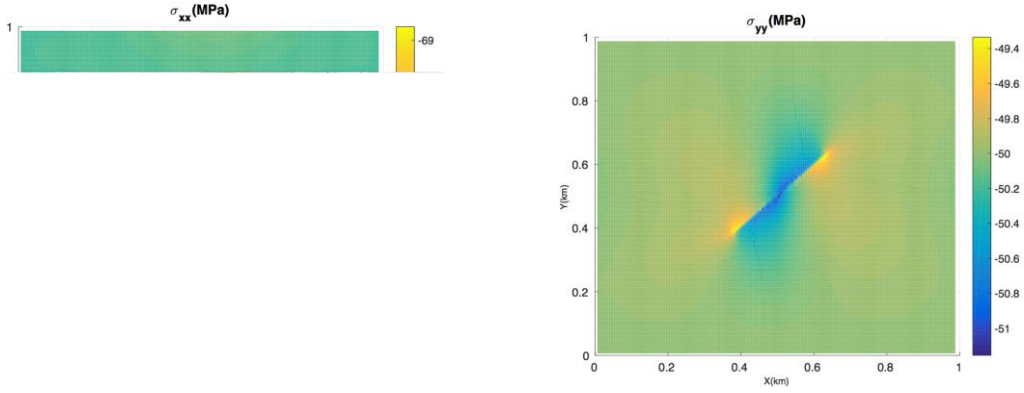

Figure 8: Numerical simulations of poro-elastic flow evolution (t = 1.74x10^4 sec after injection). The poro-elastic stress components σ_{xx} and σ_{yy} are shown in the left and right figures, respectively.

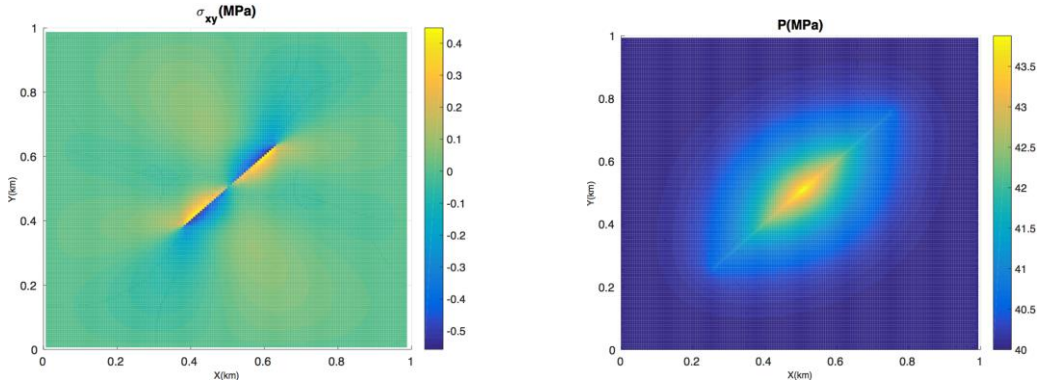

Figure 9: Numerical simulations of poro-elastic flow evolution (t = 1.7x10^4 sec after injection). The poro-elastic stress components σ_{xy} and the pressure field are shown in the left and right figures, respectively.

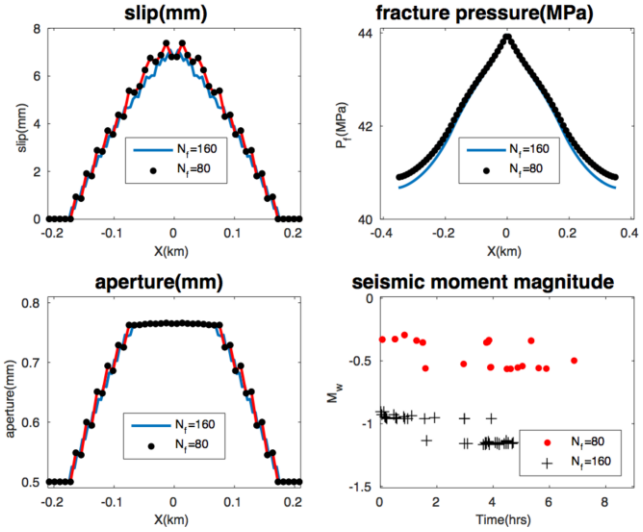

Figure 10: Numerical simulations of poro-elastic flow evolution along the fracture. The solutions for slip, pressure, aperture and M_w are compared for two grid resolutions (N_f=80, 160). The solutions are compared for same extent of shear failure propagation along the fracture. Shown on the top, in the order from left to right, are profiles of slip and fracture fluid pressure. On the bottom, in the order from left to right, the hydraulic aperture and seismic moment magnitude histories are shown.

Results of a simulation with a time step size of 10 sec are presented in figures 7-10. Displacement, stress and pressure solutions at time t = 1.7x10^4 sec after the beginning of injection are depicted in figures 7-9. From figure 9 one can observe a monotonous pressure field developing around the fracture, which reduces the effective compressive force in the region above and below the oblique fracture manifold and thus affects the displacement field (which is manifested by the solution shown in figure 7). Further, the displacement field near the fracture manifold is also affected by shear failure.

For transient studies, however, the presented model is grid resolution dependent. Shown on top of figure 10, in the order from left to right, are profiles of slip and pressure along the fracture line at different times for the two fracture resolutions N_f=80 and N_f=160, such that the fracture propagation is the same in both cases. On the bottom of figure 10, again in the order from left to right, the hydraulic aperture and seismic moment history along the fracture line are shown. While the fracture propagation speeds are different, it can be observed that the slip and aperture solutions are similar for the two grid resolutions, if the results are compared for the same extent of fracture propagation. Figure 11 depicts the frequency of events with magnitude larger than M_w for N_f = 80. It can be observed that it follows an approximate linear decay with a slope of 2.23 (b-value), which verifies a Gutenberg-Richter law.

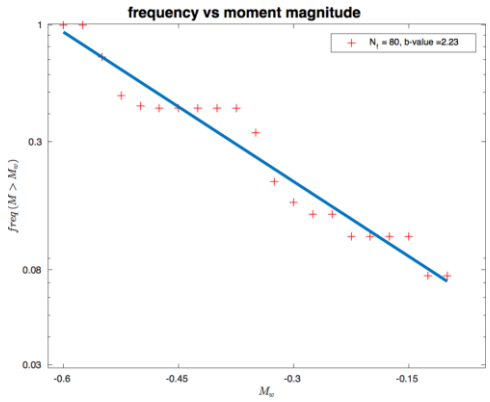

Figure 11: Frequency (freq(M>M_w)) of events with magnitude larger than M_w. The semi-logarithmic plot depicts an approximate linear decay with a slope of 2.23 (also denoted as b-value).

5. CONCLUSION

A computational modeling framework for poro-elastic coupling of flow and mechanics with shear failure along pre-existing fracture manifolds is presented. A finite volume method for both flow and mechanics is employed and a sequential iterative solver together with the fixed stress approach is used for the coupled problem. The computational efficiency is improved by exploiting the properties of the discrete system for the mechanics. Further, a Gauss-Seidel preconditioner is employed in a small region surrounding the failing fracture segments in order to improve the initial guess for the multigrid solver. The new framework was successfully validated by comparing numerical results of the Mandel problem with corresponding analytical solutions. However, the final test case with a single oblique fracture reveals that failure propagation speed and seismic magnitude frequency depend on the grid resolution.

REFERENCES

1. Castelletto, N., White, J. A., and Tchelepi, H. A.: Accuracy and Convergence Properties of Fixed-stress Iterative Solution of Two-way Coupled Poromechanics, *International Journal for Numerical and Analytical Methods in Geomechanics* **39**, (2015), 1593-1618.

2. Kim, J., and Tchelepi, H. A., and Juanes, R.: Stability, Accuracy and Efficiency of Sequential Methods for Coupled Flow and Geomechanics , *SPE Journal* **16(2)**, (2011), 249-262.

3. Kim, J., and Tchelepi, H. A., and Juanes, R.: Stability and Convergence of Sequential Methods for Coupled Flow and Geomechanics: Fixed-stress and Fixed-strain Splits, *Computer Methods in Applied Mechanics and Engineering* **200(13 - 16)**, (2011), 1591-1606.

4. Kim, J., and Tchelepi, H. A., and Juanes, R.: Stability and Convergence of Sequential Methods for Coupled Flow and Geomechanics: Drained and Undrained Splits, *Computer Methods in Applied Mechanics and Engineering* **200(13 - 16)**, (2011), 2094-2116.

5. Mikelic, A., J., and Wheeler, M. F.: Stability and Convergence of Iterative Coupling for Coupled Flow and Geomechanics, *Computational Geosciences* **17(3)**, (2013), 455-461.

6. Deb, R., and Jenny, P.: Modeling of Failure Along Predefined Planes in Fractured Reservoirs, *Proceedings*, 39th Workshop on Geothermal Reservoir Engineering, Stanford University, Stanford, CA (2014).

7. Deb, R., and Jenny, P.: Numerical Modeling of Flow Induced Shear Failure in Fractured Reservoirs, *Proceedings*, 40th Workshop on Geothermal Reservoir Engineering, Stanford University, Stanford, CA (2015).

8. Abousleiman, Y., Cheng, A. H. D., Cui, L., Detournay, E., and Roegiers, J. C.: Mandel's Problem Revisited, *Geotechnique* **46**, (1996), 187-195.

9. Gibson, R. E., Knight, K., and Taylor, P. W.: A Critical Experiment to Examine Theories of Three-dimensional Consolidation, *Proc. Eur. Conf. Soil Mech* **1**, 69-76.

10. McClure, M., and Horne, R.: Investigation of Injection Induced Seismicity Using a Coupled Fluid Flow and Rate/State Friction Model, *Proceedings*, 36th Workshop on Geothermal Reservoir Engineering, Stanford University, Stanford, CA (2011).

11. Hanks, T., and Kanamori, H.: A Moment Magnitude Scale., *Journal of Geophysical Research*, **84(B5)**, (1979), 2348-2350.

12. Wills-Richards, J., Watanabe, J. K., and Takahashi, H.: Progress Towards a Stochastic Rock Mechanics Model of Engineered Geothermal Systems, *Journal of Geophysical Research*, **101**, (1996), B12305.

13. Deb, R., and Jenny, P.: Finite Volume Based Modeling of Flow Induced Shear Failure Along Fracture Manifolds. *To be submitted.*